Supporting Information

Decoding the charge carrier dynamics in triple cation based perovskites solar cells

Mohd Taukeer Khan,[1,*] Naveen Harindu Hemasiri,[2] Samrana Kazim,[2,3] Shahzada Ahmad[2,3*]

[1]Department of Physics, Faculty of Science, Islamic University of Madinah, Prince Naifbin Abdulaziz, Al Jamiah, Madinah 42351, Kingdom of Saudi Arabia

[2]BCMaterials, Basque Center for Materials, Applications and Nanostructures, UPV/EHU Science Park, 48940, Leioa, Spain

[3]IKERBASQUE, Basque Foundation for Science, 48009, Bilbao, Spain

*Correspondence: shahzada.ahmad@bcmaterials.net; khanmtk@iu.edu.sa

1. Variation of fitting parameters with applied bias

EIS was analyzed by the equivalent circuit (EC) shown in Figure 2d. In EC R_S ascribed to the series resistance of contacts for electrical measurements and was found to be in the range of 9 – 10 Ω. The capacitance C_1 corresponds to geometrical capacitance and bulk dielectric relaxation of the perovskites layer was determined from CPE1 through the relation [1]:

$$C_1 = \left[\left(\frac{1}{R_S} + \frac{1}{R_1} \right)^{p_1 - 1} T_1 \right]^{1/p_1}$$

The capacitance C_2 corresponds to low-frequency mechanisms including ionic transport, interfacial charge accumulation, and transport and was evaluated from CPE2 through the relation:

$$C_2 = \left[\left(\frac{1}{R_S + R_1} + \frac{1}{R_2} \right)^{p_2 - 1} T_2 \right]^{1/p_2}$$

The time constant τ_1 and τ_2 were calculated from the relation: $\tau = RC$ by using corresponding values of resistance and capacitance.

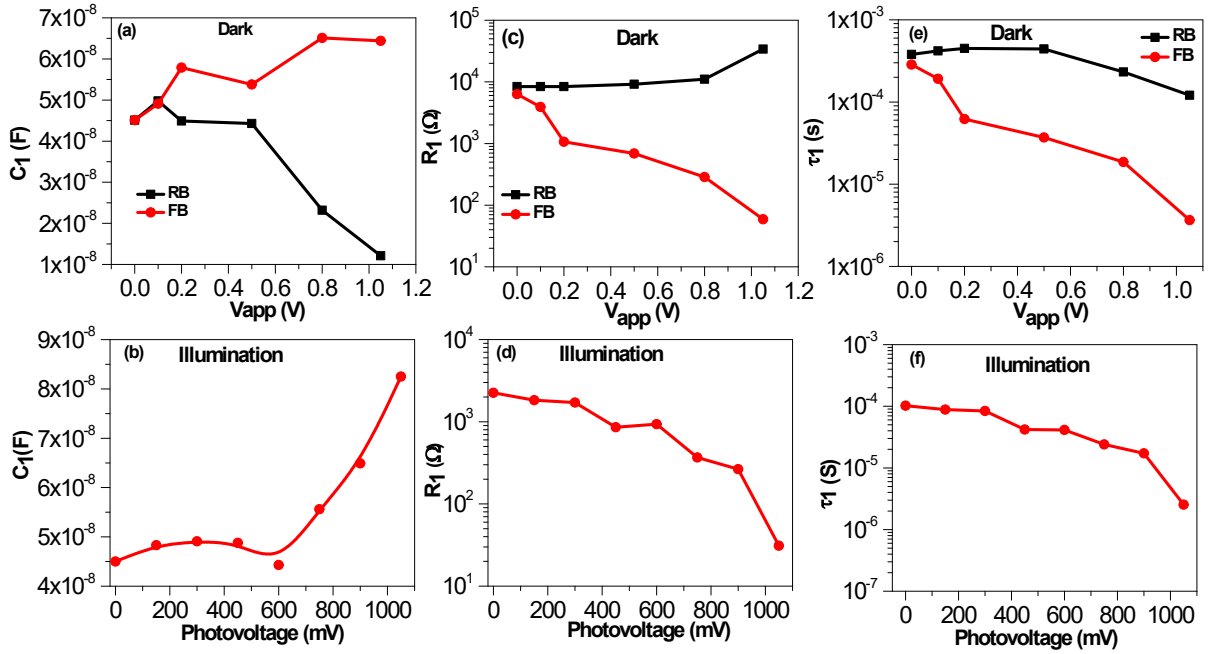

Figure S1. Variation of geometrical capacitance C_1 (a, b), charge transport resistance R_1 (c, d), and time constant τ_1 (e, f) as a function of applied bias and photovoltage.

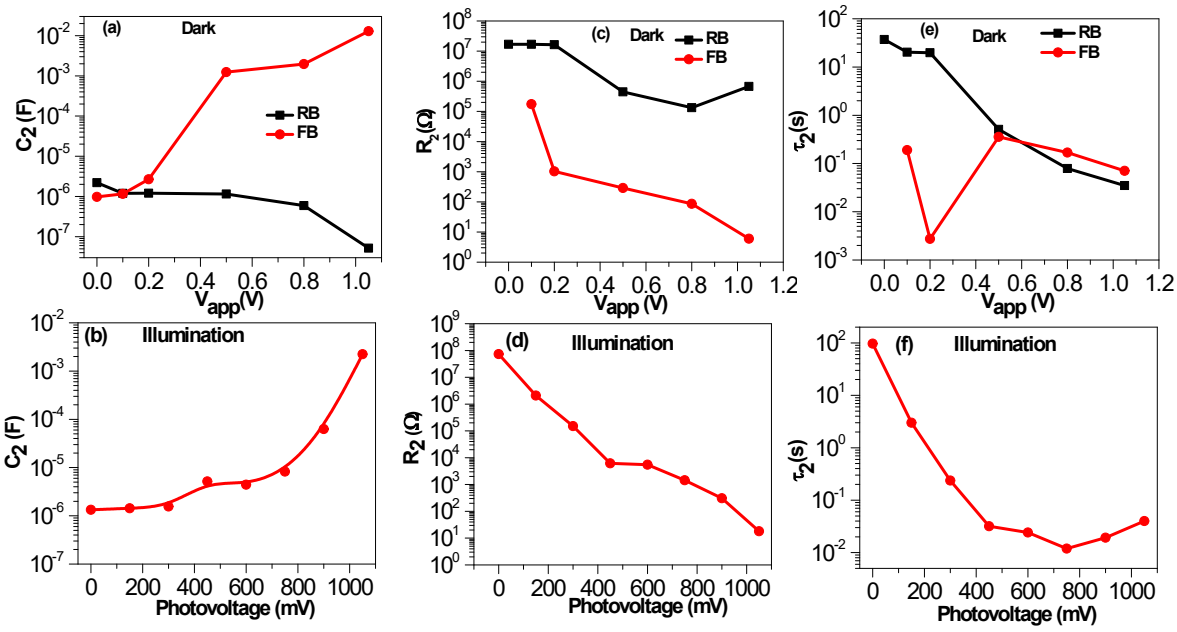

Figure S2. Variation of interfacial capacitance C_2 (a, b), recombination resistance R_1 (c, d), and time constant τ_2 (e, f) as a function of applied bias and photovoltage.

2. Dielectric constant measurement

Room temperature *C-f* spectra of perovskites layer sandwiched between FTO and Au electrodes are shown in Fig. S3. The relative dielectric constant (ε_r) of the perovskites layer was evaluated to be 44 through the relation: $C = \varepsilon_0 \varepsilon_r A/d$.

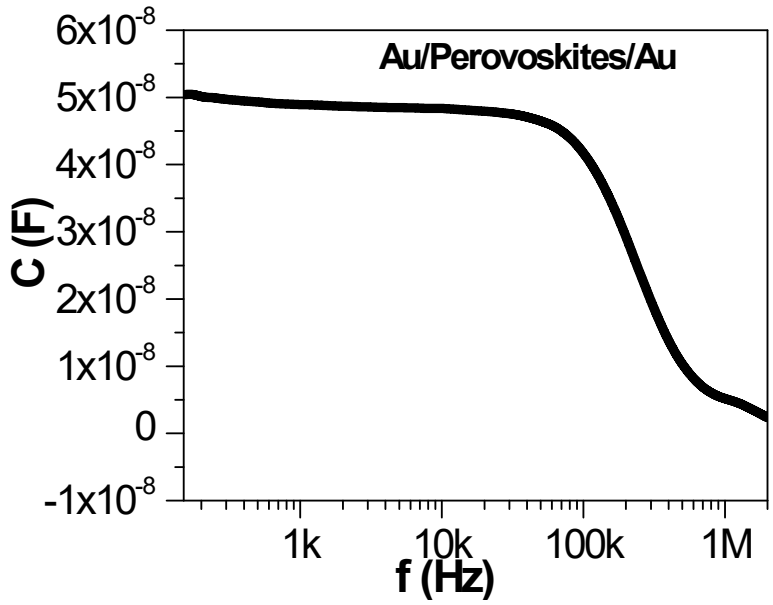

Figure S3. *C-f* spectra of FTO/perovskites/Au at room temperature.

3. Evaluation of accumulated ionic concentration at the interface

The variation of accumulation capacitance at the perovskites/TiO_2 interface as a function of photovoltage (illumination) is illustrated in Fig. S4.

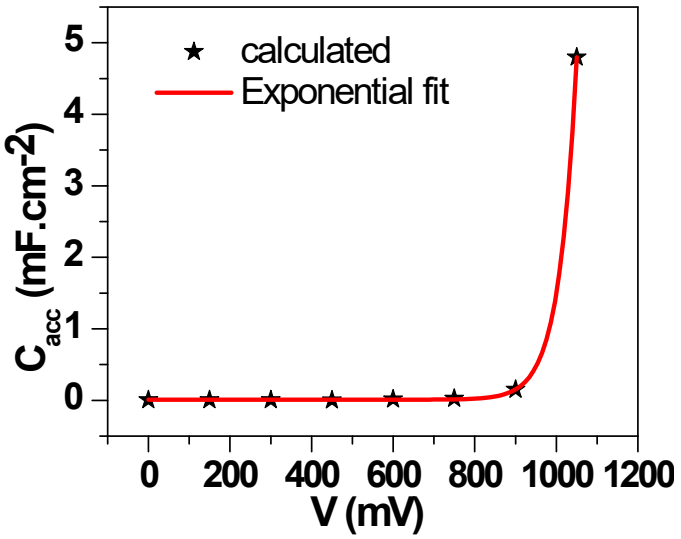

Fig. S4 Exponential fit (solid red line) of the evolution of accumulation capacitance as a function of photovoltage.

4. Temperature-dependent XRD perovskite film

Temperature-dependent X-ray diffraction (XRD) pattern of triple cation $Cs_{0.1}(FAPbI_3)_{0.81}(MAPbBr_3)_{0.09}$ perovskite films was measured in the temperature range 30 ºC – 150 ºC to check phase transition. With an increase of temperature above 90 ºC, the intensity of peak corresponds to PbI_2 i.e. (101) increases indicating degradation of perovskites layer with temperature. No change in structure can be observed in the investigated *J-V* and immittance spectroscopy temperature range, confirming the change in electrical properties with temperature is not attributed to phase transitions in the perovskites layer.

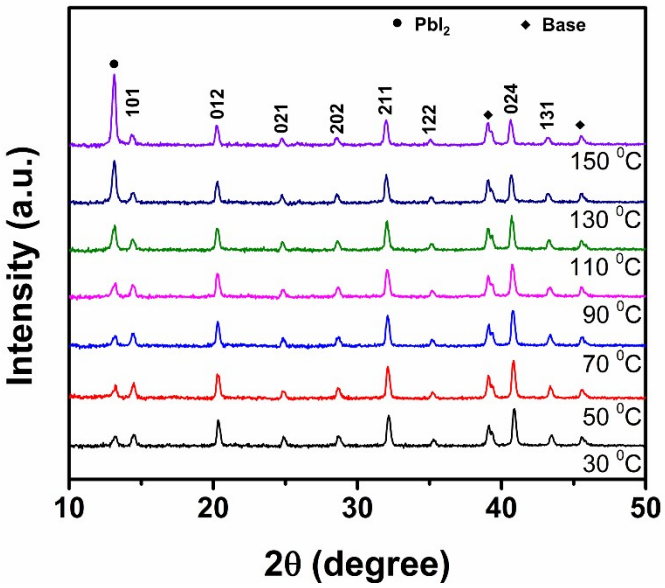

Figure S5. Temperature-dependent XRD of $Cs_{0.1}(FAPbI_3)_{0.81}(MAPbBr_3)_{0.09}$ perovskite.

5. Trap density at low temperature

Figure S6 shows the trap density profile as a function of demarcation energy (Eω) evaluated through the relation:

$$N_T = \left(-f\frac{dC}{df}\right)\frac{V_{bi}}{qWk_BT}\ ,\ E_\omega = k_BT\ln\left(\frac{\beta T^2}{\omega}\right)$$

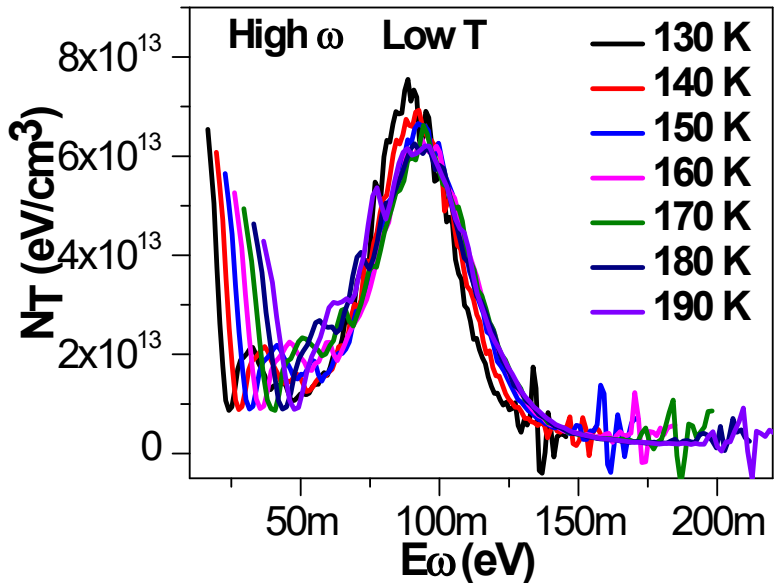

Figure S6. The temperature-dependent density of traps at low frequencies.

Table S1. Comparison of transport parameters extracted from thermal admittance spectroscopy.

Device	V_{bi} (V)	N_D (cm^{-3})	Trap DOS ($eV^{-1}cm^{-3}$)	E_A (meV)	ε_r	Ref.
FTO/c-TiO_2/mp-TiO_2/$Cs_{0.1}$ $(FAPbI3)_{0.81}$ $(MAPbBr_3)_{0.09}$ / Spiro-OMeTAD/Au	0.88	2.35×10^{21}	7.60×10^{13} 2.45×10^{15}	91 HF LT 254 LF HT	44	Present work
FTO/c-TiO_2/mp-TiO_2/ $(FAPbI_3)_{0.85}$ $(MAPbBr_3)_{0.15}$/ Spiro-OMeTAD/Au	1.05		8.84×10^{16}	124	21	3
FTO/c-TiO_2/mp-TiO_2/ $MAPbI_3$/Spiro-MeTAD/Au	0.69		1.37×10^{17}	83	32	
FTO/c-TiO_2/mp-TiO_2/ $MAPbI_3$/Spiro-MeTAD/Au			2.76×10^{18} 5.57×10^{17}	17 21	30	4
FTO/c-TiO_2/mp-TiO_2/ $MAPbI_3$/Spiro-MeTAD /Au	1.0	1.4×10^{18}		250	32.5	5
FTO/c-TiO_2/$MAPbI_3$/ Spiro- MeTAD/Au		2.4×10^{17}		450		
ITO/PEDOT/$MAPbI_3$/ $PC_{61}BM$/C_{60} /BCP/Al			1×10^{17}			6
FTO/PEDOT/$MAPbI_3$/PCBM/BCP		6.93×10^{14}				7
ITO/PEDOT/$MAPbI_x$ Cl_{3-x}/ $PC_{61}BM$/ BCP/Ag		----------	----------	390	22	8
ITO/PTAA/$MAPbI_xCl_{3-x}$/$PC_{61}BM$/ BCP/Ag				180		
FTO/TiO_2/$MAPbI_xCl_{3-x}$/P3HT/Au			3×10^{16}	660 240	18	9
FTO/TiO_2/$MAPbI_{3-x}Cl_x$/spiro/Au	1.19	1.8×10^{17}				10
ITO/PTAA/ $FAPbI_3$/ $PC_{61}BM$/BCP/Au	1.3	2.5×10^{16}			15	11
ITO/PTAA/ $MAPbI_3$/ $PC_{61}BM$/BCP/Au	1.0	2.8×10^{16}			24	
FTO/SnO_2/C_{60}-SAM/ $MA_{0.7}FA_{0.3}PbI_3$/spiro-OMeTAD/Au				172	32.5	12
ITO/PEDOT:PSS/$MA0_{.7}$ $FA_{0.3}PbI_3$ /C_{60}/BCP/Ag				19 363	26	
ITO/PTAA/$MA0_{.7}FA_{0.3}PbI_3$ /C_{60} /BCP /Ag				371	37	
ITO/PEDOT:PSS/$MAPbI_3$ /PCBM /Ca	1.0	1.2×10^{16}				13
ITO/PEDOT:PSS/$MAPbI_3$ /PCBM /Cr_2O_3/Cr	0.79	1.3×10^{16}				

Supplementary References

1. Daming Zheng, Tao Zhu, and Thierry Pauporté, Using Monovalent- to Trivalent-Cation Hybrid Perovskites for Producing High-Efficiency Solar Cells: Electrical Response, Impedance, and Stability. ACS Appl. Energy Mater. 2020, **3**, 11, 10349–10361.
2. S. Ravishankar, S. Gharibzadeh, C. Roldán-Carmona, G. Grancini, Y. Lee, M. Ralaiarisoa, A. M. Asiri, N. Koch, J. Bisquert and M. K. Nazeeruddin, Joule, 2018, **2**, 788–798.
3. M. T. Khan, M Salado, A. Almohammedi, S Kazim, S Ahmad, Adv. Mater. Interfaces 2019, **6**, 1901193.
4. D. Prochowicz, P. Yadav, M. Saliba, M. Saski, S. M. Zakeeruddin, J. Lewiński, and M. Grätzel, ACS Appl. Mater. Interfaces, 2017, **9**, 28418−28425.
5. O. Almora, I. Zarazua, E. Mas-Marza, I. M.-Sero, J. Bisquert, and G. G.-Belmonte, J. Phys. Chem. Lett. 2015, **6**, 1645–1652.
6. Shao, Y., Xiao, Z., Bi, C. et al. Origin and elimination of photocurrent hysteresis by fullerene passivation in $CH_3NH_3PbI_3$ planar heterojunction solar cells. Nat Commun., 2014, **5**, 5784.
7. Dharmadasa, I.M., et al., Perovskite solar cells: a deep analysis using current–voltage and capacitance–voltage techniques. Journal of Materials Science: Materials in Electronics, 2018, **30**, 1227-1235.
8. M. T. Khan, P. Huang, A. Almohammedi, S. Kazim, S. Ahmad, Mechanistic, iScience, 2021, **24**, 102024.
9. M. Samiee, S. Konduri, B. Ganapathy, R. Kottokkaran, H. A. Abbas, A. Kitahara, P. Joshi, L. Zhang, M. Noack, and V. Dalal, Appl. Phys. Lett. 2014, **105**, 153502.
10. Guerrero, A., et al., Electrical field profile and doping in planar lead halide perovskite solar cells. Applied Physics Letters, 2014, **13**, 105.
11. M. Fischer, K. Tvingstedt, A, Baumann, and V. Dyakonov, ACS Appl. Energy Mater. 2018, **1**, 5129–5134.
12. A. Awni, Z. Song, C. Chen, C. Li, C. Wang, M. A. Razooqi, L. Chen, X. Wang, R. J. Ellingson, J. V. Li, and Y. Yan, Joule, 2020, **4**, 644-657.
13. Guerrero, A., et al., *Interfacial Degradation of Planar Lead Halide Perovskite Solar Cells.* ACS Nano, 2016, **10**, 218.